Article

Relativistic Jet Simulations of the Weibel Instability in the Slab Model to Cylindrical Jets with Helical Magnetic Fields

Ken-Ichi Nishikawa [1]*, Yosuke Mizuno [2], Jose L. Gómez [3], Ioana Duţan [4], Athina Meli [5,6], Jacek Niemiec [7], Oleh Kobzar [7], Martin Pohl [8,9], Helene Sol [10], Nicholas MacDonald [11], and Dieter H. Hartmann [12]

1 Department of Physics, Chemistry, and Mathematics, Alabama A&M University, Normal, AL 35762, USA; kenichi.nishikawa@aamu.edu
2 Institute for Theoretical Physics, Goethe University, Frankfurt am Main D-60438, Germany; mizuno@th.physik.uni-frankfurt.de
3 Instituto de Astrofísica de Andalucía, CSIC, Apartado 3004, Granada 18080, Spain; jlgomez@iaa.csic.es
4 Institute of Space Science, Atomistilor 409, Bucharest-Magurele RO-077125, Romania; ioana.dutan@gmail.com
5 Department of Physics and Astronomy, University of Gent, Proeftuinstraat 86, Gent B-9000, Belgium
6 Department of Physics and Astronomy, University of Liege, Place du 20-Août, 7 4000 Liège, Belgium; ameli@ulg.ac.be
7 Institute of Nuclear Physics PAN, ul. Radzikowskiego 152, Kraków 31-342, Poland; Jacek.Niemiec@ifj.edu.pl (J.N.); oleh.kobzar@ifj.edu.pl(O.K.)
8 Institut fur Physik und Astronomie, Universität Potsdam, Potsdam-Golm 14476, Germany; pohlmadq@gmail.com
9 DESY, Platanenallee 6, Zeuthen 15738, Germany; pohlmadq@gmail.com
10 LUTH, Observatore de Paris-Meudon, 5 place Jules Jansen, Meudon Cedex 92195, France; helene.sol@obspm.fr
11 Max-Planck-Institut für Radioastronomie, Auf dem Hügel 69, D-53121 Bonn, Germany; nmacdona@mpifr-bonn.mpg.de
12 Department of Physics and Astronomy, Clemson University, Clemson, SC 29634, USA; hdieter@g.clemson.edu
* Correspondence: knishika27@gmail.com; Tel.: +1-256-883-5446
† These authors contributed equally to this work.

Academic Editor: Emmanouil Angelakis, Markus Boettcher Jose L. Gòmez
Version November 16, 2018 submitted to Preprints

Abstract: The Particle-In-Cell (PIC) method has been developed in order to investigate microscopic phenomena, and with the advances of computing power, newly developed codes have been used for several fields such as astrophysical, magnetospheric, and solar plasmas. Its applications have grown extensively with large computing powers available such as Pleiades and Blue Water systems in the US. For astrophysical plasmas research PIC method has been utilized in several topics such as reconnection, pulsar, non-relativistic shocks, relativistic shocks, relativistic jets, etc. As one of the research topics in astrophysics, PIC simulations of relativistic jets are reviewed up to the present time with the emphasis on the physics involved in the simulations. In this review we summarize PIC simulations starting with the Weibel instability in slab models of jets and then, continuing with recent progresses on global jets with helical magnetic fields including kinetic Kelvin-Helmholtz instabilities and mushroom instabilities.

Keywords: particle-in-cell simulations; relativistic jets; the Weibel instability, kink-like instability; mushroom instability; global jets; helical magnetic fields; recollimation shocks

 doi:10.20944/preprints201811.0374.v1

1. Introduction

Relativistic jets are collimated outflows of ionized matter generated from (super massive) black holes, the collapse of the core of a massive star to form a neutron star or a black hole, the merger of binary neutron stars and neutron stars which are associated with active galactic nuclei (AGN), gamma-ray bursts (GRBs), and pulsars ([e.g., 1]). GRB jets and blazars produce the brightest electromagnetic phenomena in the universe (e.g., [2]). In spite of intensive and extensive observational and theoretical investigations, including various simulation studies, the understanding of their formation, their interaction with interstellar medium, and consequently their observable properties such as spectra, time-variabilities, time-dependent flux and polarity images (e.g., [3]) remains quite limited.

In the universe, astrophysical jets are found everywhere and exhibit a range of plasma phenomena such as propagation in the interstellar medium, generation/annihilation of magnetic fields, magnetic reconnection, turbulence, and resultant particle acceleration including generation of ultra-high energy particles. Many of the processes that determine the evolution of global relativistic jets are very complex, involving various plasma physics. Microscopic processes that occur on short spatial and temporal scales associated with plasma kinetic effects are integrated into global, large-scale dynamics, which may provide new insights into dynamics of jets. Kinetic plasma simulations are performed using PIC codes, with the intent to advance the knowledge of properties of global relativistic jets and associated phenomena such as particle acceleration and kinetic magnetic reconnection, which cannot be investigated with fluid models (i.e., relativistic magnetohydrodynamic (RMHD) simulations).

Particle-in-cell (PIC) simulations can provide us with new insights into the microscopic processes in jet dynamics. Recent PIC simulations show that particle acceleration occurs due to kinetic instabilities such as the electron and ion Weibel instabilities [e.g., 4–26]. In general, these simulations confirm that the Weibel instability is dominant among kinetic instabilities in weakly or nonmagnetized plasma [27]. The resultant current filaments and magnetic fields [e.g., 28] accelerate electrons [e.g., 12] and cosmic rays, which affect the pre-shock medium [29].

In order to create a shock, a relativistic plasma flow is injected from one end of the computational grid and reflected from a boundary at the opposite end for instance, 1D simulations by [30,31], 2D simulations by [e.g., 14,15,19,25,26,32], and 3D simulations by [33,34]. In this method, two identical counter-streaming beams collide, which reduces by one-half the number of calculations to investigate particle acceleration at the termination shocks, where only one forward moving shock (FS) is generated. In these settings the backward (reverse) shock (RS) is indistinguishable from FS. In this review the works where a jet is injected into an ambient plasma are presented, so that FS and RS shock structure is fully modelled. In this way the jet-to-ambient density ratio is selected as appropriate plasma conditions of AGN and GRB jets. The shock formation processes can be investigated temporally and spatially. PIC simulations where jets are reflected at the simulation boundary are reviewed including the generation of high-energy particles by [35].

A contact discontinuity (CD) is generated due to deceleration of the jet flow by the ambient plasma. The CD is the location where the electromagnetic field, the velocity of the jet, and the ambient plasmas are similar but the density changes. FS and RS propagate away from the CD into the jet and ambient plasmas (in the CD frame) [18,21–23]. Ardaneh et al.[22] have illustrated that FS, RS and one CD split up the jet and ambient plasma into four regions: (1) unshocked ambient, (2) shocked ambient, (3) shocked jet, and (4) unshocked jet.

In this review we summarize our previous studies from slab jet case to global cylindrical jet case briefly and present new three-dimensional simulation results for an electron-positron jet injected into an electron-positron plasma using a long simulation grid in jet propagation direction. A leading and trailing shock system develops with strong electromagnetic fields accompanying the trailing shock.

Preprints (www.preprints.org) | NOT PEER-REVIEWED | Posted: 16 November 2018 doi:10.20944/preprints201811.0374.v1

2. PIC Simulations in a Slab Model

It is natural to start to perform PIC simulations in a slab model where jets are injected into the whole simulation system. Since we use the periodic boundary conditions transverse direction to the jets, we are simulating a part of jets without taking into the boundary between jets and ambient plasmas. The instabilities generated between jets and ambient plasmas are described later.

2.1. Simulation of the Weibel Instability

The Weibel instability is a plasma instability which occurs in homogeneous or nearly homogeneous plasmas where an anisotropy exists in momentum (velocity) space[27]. The Weibel instability is often referred to as a filamantation instability [36].

The mechanisms of Weibel instability growth are explained as following: Suppose a field $\mathbf{B} = B_z \cos ky$ is spontaneously generated by thermal fluctuation. Here, k is a wave number, the x, y and z are the coordinates and electrons travel along the x direction. The Lorentz force $(-e\mathbf{v} \times \mathbf{B})$ then bends the electron trajectories (travelling along the x direction) along the y direction with the result that electrons congregate. The resultant current $\mathbf{j} = -en\mathbf{v}_e$ sheets (filaments) create magnetic field that enhances the original field and thus a perturbation grows.

The Weibel instability is also common in astrophysical plasmas, such as collisionless shock formation in jets, supernova remnants and γ-ray bursts.

2.1.1. Simulation Settings

The code used in this study is an MPI-based parallel version of the relativistic particle-in-cell (RPIC) code TRISTAN [5,37,38]. The simulations have been performed using a grid with $(L_x, L_y, L_z) = (4005, 131, 131)$ cells and a total of $\sim$1 billion particles (12 particles/cell/species for the ambient plasma) in the active grid. The electron skin depth, $\lambda_s = c/\omega_{pe} = 10.0\Delta$, where $\omega_{pe} = (e^2 n_a/\epsilon_0 m_e)^{1/2}$ is the electron plasma frequency and the electron Debye length λ_D is half of the cell size, Δ. This computational system length is six times longer than in the previous simulations [12,39]. The jet-electron number density in the simulation reference frame is $0.676n_a$, where n_a is the ambient electron density, and the jet Lorentz factor is $\gamma_j = 15$. The jet-electron/positron thermal velocity is $v_{j,th} = 0.014c$ in the jet reference frame, where $c = 1$ is the speed of light. The electron/positron thermal velocity in the ambient plasma is $v_{a,th} = 0.05c$. As in our previous work [e.g., 12], the jet is injected in a plane across the computational grid located at $x = 25\Delta$ in order to eliminate artificial effects associated with the boundary at $x = x_{min}$. Radiating boundary conditions are used on the planes at $x = x_{min}$ and $x = x_{max}$ and periodic boundary conditions on all transverse boundaries [37]. The jet makes contact with the ambient plasma at a two-dimensional interface spanning the whole computational domain in the $y - z$ plane. In this way, a small portion of whole jets is studied, that includes the spatial development of nonlinear saturation and dissipation from the injection point to the jet front composed of the fastest moving jet particles. moving jet particles. Therefore, the boundary between jets and ambient plasma is not taken into account, which will be described later.

2.1.2. Simulation Results

Figures 1(a) and (b) show the averaged (in the $y - z$ plane) (a) jet (red), ambient (blue), and total (black) electron density and (b) electromagnetic field energy divided by the total jet kinetic energy ($E_t^j = \sum_{i=e,p} m_i c^2(\gamma_j - 1)$) at $t = 3250\omega_{pe}^{-1}$. Here, "e" and "p" denote electron and positron. Positron density profiles are similar to electron profiles due to the same mass. However, for the electron-ion jets, the densities of electron and ions are slightly different, which generate the double layers [21,23**?**]. Ambient particles are moved with jet particles $x/\Delta \sim 500$. By $t = 3250\omega_{pe}^{-1}$, the density has evolved into a two-step plateau behind the jet front which is similar to the electron-ion jet cases [21,23**?**]. The maximum density in this shocked region is about three times the initial ambient density. The jet-particle density remains nearly constant up to near the front of the jet. The careful comparisons

Preprints (www.preprints.org) | NOT PEER-REVIEWED | Posted: 16 November 2018 doi:10.20944/preprints201811.0374.v1

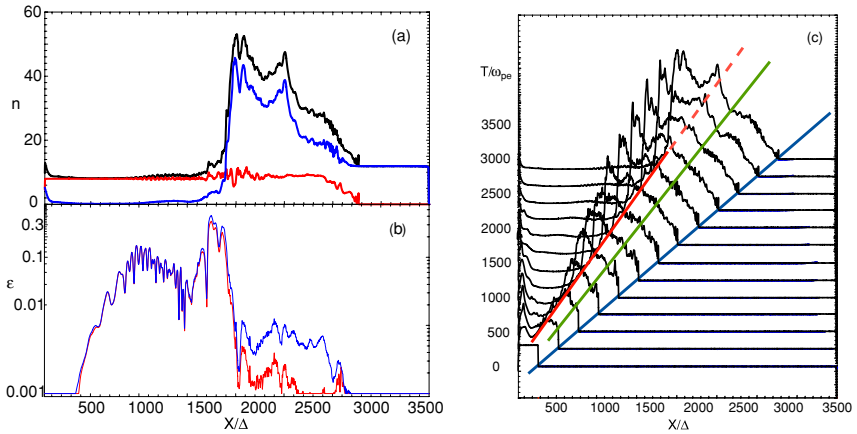

Figure 1. Averaged values of (a) jet (red), ambient (blue), and total (black) electron density, and (b) electric (red) and magnetic (blue) field energy divided by the jet kinetic energy at $t = 3250\omega_{pe}^{-1}$. Panel (c) shows the evolution of the total electron density in time intervals of $\delta t = 250\omega_{\rm pe}^{-1}$. Diagonal lines indicate motion of the jet front (blue: $\leq c$), predicted CD speed (green: $\sim 0.76c$), and trailing density jump (red: $\sim 0.56c$). Adapted from Fig. 1 in [18].

reveal the differences between the pair jets and electron-ion jets [21–23]. The differences come due to the double layers generated in the trailing and leading edges in electron-ion jets.

The growth of the Weibel instability create current filaments and strong electromagnetic fields in the trailing shock region. Since the nonlinear stage is formed in this simulation, the electromagnetic fields are about four times larger than that seen previously using a much shorter grid system ($L_{\rm x} = 640\Delta$). At $t = 3250\omega_{pe}^{-1}$, the electromagnetic fields are largest at $x/\Delta \sim 1700$, and decline by about one order of magnitude beyond $x/\Delta = 2300$ in the shocked region [12,39].

Figure 1(c) shows the total electron density plotted at time intervals of $\delta t = 250\omega_{\rm pe}^{-1}$. The jet front propagates with the initial jet speed ($\leq c$). Since anomalous resistivity exists in PIC simulations, sharp RMHD-simulation shock surfaces are not generated [e.g., 40]. A leading shock region (linear density increase) moves with a speed between the fastest moving jet particles $\leq c$ and a predicted CD speed of $\sim 0.76c$. A CD region consisting of mixed ambient and jet particles moves at a speed between $\sim 0.76c$ and the trailing density jump speed $\sim 0.56c$. A trailing shock region moves with speed $\sim 0.56c$; note the modest density increase just behind the large trailing density jump. Similar shock structures and their velocities for the electron-ion jets are discussed in [21–23].

It is important to show the differences between the reflection and injection models.

The shock is set up by reflecting a cold "upstream" flow from a conducting wall located at $x = 0$ (Figure 1). The interaction between the incoming beam (that propagates along $-\mathbf{x}$) and the reflected beam triggers the formation of a shock, which moves away from the wall along $+\mathbf{x}$) [33]. This setup is equivalent to the head-on collision of two identical plasma shells, which would form a forward and reverse shock and a contact discontinuity. Here, we follow only one of these shocks, and replace the contact discontinuity with the conductingwall. The simulation is performed in the "wall" frame, where the "downstream" plasma behind the shock is at rest.

In 3D, they employ periodic boundary conditions both in y and in z. Each computational cell is initialized with four particles (two per species) in 2D and with two particles (one per species) in 3D. They have performed limited experiments with a larger number of particles per cell (up to eight per species in 2D), obtaining essentially the same results.

Their 3D structure is shown in Figure 2, for a relativistic electron-positron shock with magnetization $\sigma = 0$ (top panel) and $\sigma = 10^{-3}$ (bottom panel). The background magnetic field B_0 is oriented here along the z direction, in the same way as for our 2D simulations. The yz slice of the magnetic energy fraction in Figure 2(c) shows that for $\sigma = 10^{-3}$ the magnetic field ahead of the

Preprints (www.preprints.org) | NOT PEER-REVIEWED | Posted: 16 November 2018 doi:10.20944/preprints201811.0374.v1

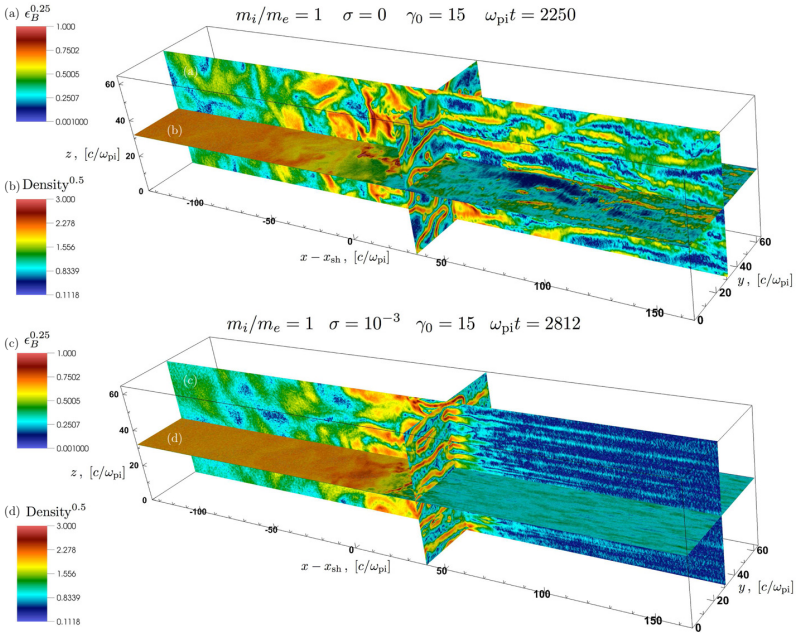

Figure 2. Structure of the flow, from the 3D simulation of an electron-positron shock with magnetization $\sigma = 0$ (top) or $\sigma = 10^{-3}$ (bottom). The xy slice shows the particle density (with color scale stretched for clarity), whereas the xz and yz slices show the magnetic energy fraction $\epsilon_{\rm B}$ (with color scale stretched for clarity). Adapted from Fig. 5 in [33].

shock is primarily organized in pancakes stretched in the direction orthogonal to the background magnetic field (i.e., along y). This can be simply understood, considering that the Weibel instability is seeded by the focusing of counterstreaming particles into channels of charge and current. In the absence of a background magnetic field, the currents tend to be organized into cylindrical filaments, as demonstrated by Spitkovsky [41] and shown in the yz slice of the top panel in Figure 2. In the presence of an ordered magnetic field along z, the particles will preferentially move along the magnetic field (rather than orthogonal), so that their currents will more likely be focused at certain locations of constant z, into sheets elongated along the xy plane. This explains the structure of the magnetic turbulence ahead of the shock in the bottom panel of Figure 2, common to all the cases of weakly magnetized shocks we have investigated (i.e., $0 < \sigma \leq 10^{-1}$).

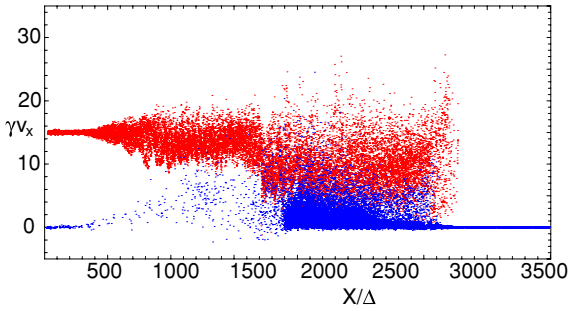

Figure 3. Phase-space distribution of jet (red) and ambient (blue) electrons at $t = 3250\omega_{pe}^{-1}$. About 18,600 electrons of both species are selected randomly. Adapted from Fig. 2 in [18].

Figure 3 shows the phase-space distribution of jet (red) and ambient (blue) electrons at $t = 3250\omega_{pe}^{-1}$ and confirms the shock-structure interpretation. The electrons injected with $\gamma v_{\rm x} \sim 15$ become

 doi:10.20944/preprints201811.0374.v1

thermalized due to Weibel instabililty induced interactions. The swept-up ambient electrons (blue) are heated by interaction with the jet electrons. Some ambient electrons are strongly accelerated.

This simulation shows that the shocks are excited through the injection of a relativistic jet into ambient plasma, leading to two distinct shocks (referred to as the trailing shock and leading shock) and a contact discontinuity. It should be noted that in the simulations where jets are reflected on the simulation boundary do not show the structure of a leading shock, a contact discontinuity, and a trailing (reverse) shock.

For the electron-ion jet case, the mass ratio of $m_i/m_e = 16$ therefore, the evolution of density (shock) structures are different from those in the electron-positron jet ($m_i/m_e = 1$) [22,23]. **Furthermore, the double layers generated in the trailing and leading edges then accelerate the electrons up to the ion kinetic energy [23].**

2.2. Simulation of Jets with Velocity-Shears

In a slab jet model the generation of shocks have been studied extensively. However, the velocity shears between jet and ambient medium need to be taken into account, where outflow interaction with an ambient medium induces velocity shearing.

In particular, the Kelvin–Helmholtz instability (KHI) has been investigated on the macroscopic level as a means to generating magnetic fields in the presence of strong relativistic velocity shears in AGNs and GRB jets [e.g., 42–46]. Recently, PIC simulations have been employed to study magnetic field generation and particle acceleration in velocity shears at the microscopic level using counter-streaming setups. Here the shear interactions are associated with the kinetic Kelvin–Helmholtz instability (kKHI), also referred to as the electron-scale Kelvin–Helmholtz instability [ESKHI; e.g., 47–53].

Alves et al. [54] have presented the shear surface instability that occurs in the plane perpendicular to that of the ESKHI. These new unstable modes explain the transverse dynamics and structures observed in PIC simulations in [47,49,52,55]. They label this effect the mushroom instability (MI) due to the mushroom-like structures that emerge in the electron density, in particular 2D simulation. In 3D simulations the shape of mushroom is not seen clearly, but it grows strong [56].

Multidimensional PIC simulations confirm the analytic results and further show the appearance of mushroom-like electron density structures in the nonlinear stage of the instability, similar to those observed in the Rayleigh Taylor instability despite the great disparity in scales and different underlying physics [54,56]. This transverse electron-scale instability may play an important role in relativistic and supersonic sheared flow scenarios, which are stable at the (magneto)hydrodynamic level, which will be shown later in a cylindrical geometry. Macroscopic ($\gg c/\omega_{pe}$) fields are shown to be generated by this microscopic shear instability, which are relevant for generation of DC electric field and toroidal magnetic field (B_ϕ), particle acceleration, radiation emission, and to seed magnetohydrodynamic processes at long time scales [54,56].

2.2.1. Spine-Sheath (Two-Components) Jet Setup

In this simulation a spine-sheath (two-component) plasma jet structure is studied using the counter-streaming plasma setup implemented in simulations by [47,49–53]. In the setup, a jet spine (core) with velocity γ_{core} propagates in the positive x direction in the middle of the computational box. The upper and lower quarters of the numerical grid contain a sheath plasma that can be stationary or moving with velocity v_{sheath} in the positive x direction [48,55]. This model is similar to the setup in the RMHD simulations [44] that used a cylindrical jet spine (core).

Nishikawa et al. [55] performed 3D PIC simulations of the kKHI and MI for both electron–positron and electron–proton plasmas. The processes studied here are inspired from the jets from AGNs and GRBs that are expected to have velocity shears between faster spine (core) and slower sheath wind (stationary ambient plasmas). In these simulations, large velocity shears are studied with relative Lorentz factors of 1.5, 5, and 15.

Preprints (www.preprints.org) | NOT PEER-REVIEWED | Posted: 16 November 2018 doi:10.20944/preprints201811.0374.v1

Figure 4 shows the structure of the B_y component of the magnetic field in the $y-z$ plane (jet flows out of the page) at the midpoint of the simulation box, $x = 500\Delta$, and 1D cuts along the z axis showing the magnitude and direction of the magnetic field components at the midpoint of the simulation box, $x = 500\Delta$ and $y = 100\Delta$ for the $e^- - p^+$ case at simulation time $t = 300\omega_{pe}^{-1}$, with $\gamma_{jt} = 15$ [55]. In the $e^- - p^+$ case, magnetic fields appear relatively uniform at the velocity shear surfaces along the transverse y direction just as was seen at the velocity shear surfaces along the parallel x direction, with almost no transverse fluctuations visible in the magnetic field (small fluctuations in the y direction over distances on the order of $\sim 10\Delta$ are visible in the currents, whereas small longitudinal mode fluctuations in the x direction occur over distances $\sim 100\Delta$. This shows that MI generates DC fields in the transverse direction see also the results in global jet simulations without helical magnetic fields [56].

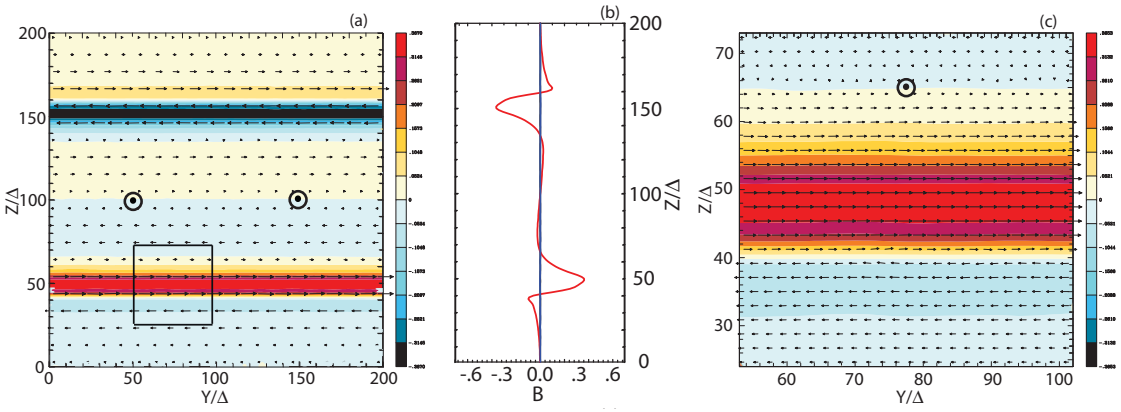

Figure 4. Magnetic field structure transverse to the flow direction for $\gamma_{jt} = 15$ is shown in the $y-z$ plane (jet flows out of the page) at the center of the simulation box, $x = 500\Delta$ for the $e^- - p^+$ case. The small arrows show the magnetic field direction in the transverse plane (the arrow length is not scaled to the magnetic field strength). 1D cuts along the z axis of magnetic field components B_x (black), B_y (red), and B_z (blue) are plotted at $x = 500\Delta$ and $y = 100\Delta$ for (b) the $e^- - p^+$ case. Note that the magnetic field strength scales in panels (a) (± 0.367) is different. An enlargement of the shear surface structure in the $y-z$ plane contained within the squares in the left panels is shown in the panels (c) to the right. Adapted from Fig. 6 in Nishikawa et al. [55].

For the electron–positron case, the magnetic field alternates in both the y and z directions and these transverse fluctuations occur over distances on the order of $\sim 100\Delta$, whereas longitudinal mode fluctuations in the x direction occur over distances $\sim 100\Delta$ [55]. The 1D cuts show that the B_y field component dominates in the $e^- - p^+$ case, that the B_y field component is about an order of magnitude smaller for the $e^\pm$ case, and that the B_z component is significant for the $e^\pm$ case. The 1D cuts also show that there is magnetic field sign reversal on either side of the maximum that is relatively small for the $e^- - p^+$ case but is much more significant for the $e^\pm$ case. More details are revealed by the enlargement of the region contained in the squares. For the $e^- - p^+$ case, the generated relatively uniform DC magnetic field is symmetric about the velocity shear surface, e.g., note that $B_y > 0$ immediately around the shear surface and$B_y < 0$ in the jet and ambient plasmas at somewhat larger distances from the shear surface. It should be noted that this DC magnetic field is generated by the mushroom instability and saturated at this time. The MI is generated in the global electron-proton jet, which pinched the jet [56]. On the other hand, for the $e^\pm$case the generated AC magnetic field resides largely on the jet side of the velocity shear surface. This phenomenon is also found in the global jet simulation [56] and outflow simulation [57].

The strong electric and magnetic fields in the velocity shear zone will also be conducive to particle acceleration. The simulations are too short for definitive statements on the efficacy of the process and the resulting spectra. Also, the organization of the field in compact regions will complicate the interpretation of emission spectra, and a spatially resolved treatment of particle acceleration and transport would be mandatory for a realistic assessment, which is beyond the scope of this review

Preprints (www.preprints.org) | NOT PEER-REVIEWED | Posted: 16 November 2018 doi:10.20944/preprints201811.0374.v1

paper. Relativistic electrons, for example, will suffer little synchrotron energy loss outside of the thin layer of strong magnetic field. Thus synchrotron emissivity will be dominated by the shear layer and in general, this emissivity will depend on how efficiently electrons can flow in and out of the shear layer and be accelerated in the regions of strong magnetic field. An immediate consequence for radiation modeling is that the energy loss time of electrons cannot be calculated with the same mean magnetic field that is used to compute emission spectra because the former includes the volume filling factor of the strong-field regions.

3. PIC Simulations of Cylindrical Jets

Since the structure of relativistic jets is intrinsically cylindrical, instabilities which occur at velocity shears are investigated in cylindrical geometry for a pair ($e^{\pm}$) and an electron-proton ($e^{-}-p^{+}$) jet. The un-magnetized jets are implemented in an ambient plasma along the x direction. Figure 5 shows isocontour images of the x component of the current along with magnetic field lines generated by the dominant kKHI for $e^{\pm}$ and $e^{-}-p^{+}$ jets. The isocontour images show that in the $e^{-}-p^{+}$ jet case currents are generated in sheet like layers and the magnetic fields are wrapped around the jet generated by the dominant MI. On the other hand, in the $e^{\pm}$ jet case many distinct current filaments are generated near the velocity shear and the individual current filaments are wrapped by the magnetic field. The clear difference in the magnetic field structure between these two cases may make it possible to distinguish different jet compositions via differences in circular and linear polarization which are seen clearly in the global jets injected into an ambient plasmas [56].

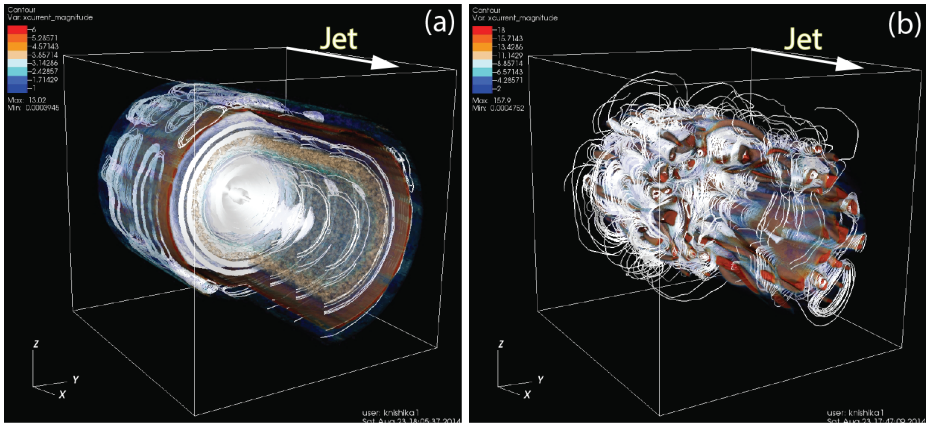

Figure 5. Isocontour plots of the J_x magnitude with magnetic filed lines (one fifth of the jet size) for (a) an $e^{-}-p^{+}$ and (b) an $ee^{\pm}$ jet at simulation time $t = 300\omega_{pe}^{-1}$. The 3D displays are clipped along the jet and perpendicular to the jet in order to view the interior. Adapted from Fig. 4 in Nishikawa et al. [58].

Recently, Alves et al.[59] consider magnetic field profiles of the form $\mathbf{B}(r) = B_0(r/R_c)e^{1-r/R_c}\mathbf{e}_\phi + B_z\mathbf{e}_z$, where R_c is the cross-sectional radius of the jet spine. They also demonstrated that toroidal magnetic field profiles that decay as $r^{-\alpha}$ (with $\alpha \geq 1$), and determined that their overall findings are not sensitive to the structure of the magnetic field far from R_c. Near the black hole, the poloidal and toroidal magnetic field components (B_z and B_α, respectively) are comparable to one another [60]. However, B_z/B_α decreases with distance from the source, and can be very small at the relevant $\sim$100 pc distances. The characteristic magnetic field amplitude (henceforth denoted as B_0) at these distances, $B_0 \sim$ mG, is quite strong in the sense that the ratio σ of the magnetic to plasma rest-mass energy densities may exceed unity. This review show the importance of macroscopic kink instabilities since strong helical magnetic fields suppress kinetic instabilities such as the Weibel instability, kKHI, and MI, however a kink-like instability more likely occurs as shown in [61**?**].

Recently, global relativistic PIC simulations are performed where a cylindrical unmagnetized jet is injected into an ambient plasma in order to investigate shock (Weibel instability) and velocity shear instabilities (kKHI and MI) simultaneously [56]. Previously, these two processes have been

Preprints (www.preprints.org) | NOT PEER-REVIEWED | Posted: 16 November 2018 doi:10.20944/preprints201811.0374.v1

investigated separately. For example, kKHI and MI have been investigated for sharp velocity shear slabs and cylindrical geometries extending across the computational grid [e.g., 55,58,59].

In this review we present the results of this new study of global relativistic jets containing helical magnetic fields. The global simulation results including velocity shears (at this time) using a small simulation system validate the use of the simulation code for the research project.

4. Simulation Setups of Global Jet Simulations

Recently global simulations are performed involving the injection of a cylindrical unmagnetized jet into an ambient plasma are performed in order to investigate shock (Weibel instability) and velocity shear instabilities (kKHI and MI) simultaneously [56]. Previously these two processes have been investigated separately. For example, kKHI and MI have been investigated for sharp velocity shear slab and cylindrical geometries extending across the computational grid (e.g.,nishikawa14b,nishikawa14c,alves18xeff). In this section we present the results of this new study of global relativistic jets containing helical magnetic fields.

Jets generated from black holes and merging neutron stats, which are then injected into the ambient interstellar medium are thought to carry helical magnetic fields. Based on this fact which are also shown in many GRMHD simulations of jet formations (e.g., [62]), global simulations of jets are injected into an ambient medium implementing helical magnetic fields near the jet orifice, (e.g., [61,63]). One of the key issues is how the helical magnetic fields affect the growth of the kKHI, the MI, and the Weibel instability. RMHD simulations demonstrated that jets containing helical magnetic fields develop kink instability, (e.g., [64–66]). Since the PIC simulations are large enough to include a kink instability, a kink-like instability is found in the pair and electron-proton jet cases (e.g., [61,63]).

4.1. Helical Magnetic Field Structure

In the simulations [61,67], cylindrical jets are injected with a helical magnetic field (see Figure 6(a)) implemented like that in RMHD simulations performed by Mizuno et al. [68].

Since the helical magnetic field is not generated with jets powered by a rotating black hole self-consistently in this simulation, a force-free helical magnetic field is implemented at the jet orifice. For initial conditions, the force-free helical magnetic field is used as described in Eqs. (1) and (2) from Mizuno et al. (2014).

The following form is used for the poloidal (B_x) and toroidal (B_ϕ) components of the magnetic field determined in the laboratory frame

$$B_x = \frac{B_0}{[1+(r/a)^2]^\alpha}, \quad B_\phi = \frac{B_0}{(r/a)[1+(r/a)^2]^\alpha}\sqrt{\frac{[1+(r/a)^2]^{2\alpha}-1-2\alpha(r/a)^2}{2\alpha-1}}, \tag{1}$$

where r is the radial position in cylindrical coordinates, B_0 parameterizes the magnetic field, a is the characteristic radius of the magnetic field (the toroidal field component is a maximum at a for constant magnetic pitch), and α is a pitch profile parameter.

In the simulations [61,67], cylindrical jets are injected with a helical magnetic field (see Figure 6(a)) implemented like that in RMHD simulations performed by Mizuno *et al.* [64]. The simulations use Cartesian coordinates. Since $\alpha = 1$ Eq. (1) is reduced to Eq. (2), and the magnetic field takes the form:

$$B_x = \frac{B_0}{[1+(r/a)^2]}, \quad B_\phi = \frac{(r/a)B_0}{[1+(r/a)^2]}. \tag{2}$$

The toroidal magnetic field is created by a current $+J_x(y,z)$ in the positive x-direction, so that defined in Cartesian coordinates:

$$B_y(y,z) = \frac{((z-z_{\rm jc})/a)B_0}{[1+(r/a)^2]}, \quad B_z(y,z) = -\frac{((y-y_{\rm jc})/a)B_0}{[1+(r/a)^2]}. \tag{3}$$

Preprints (www.preprints.org) | NOT PEER-REVIEWED | Posted: 16 November 2018 doi:10.20944/preprints201811.0374.v1

Here a is the characteristic length-scale of the helical magnetic field, $(y_{\rm jc},\, z_{\rm jc})$ is the center of the jet, and $r = \sqrt{(y-y_{\rm jc})^2 + (z-z_{\rm jc})^2}$. The chosen helicity is defined through Eq. (3), which has a left-handed polarity with positive B_0. At the jet orifice, the helical magnetic field is implemented without the motional electric fields. This corresponds to a toroidal magnetic field generated self-consistently by jet particles moving along the $+x$-direction.

The poloidal (B_x: black) and toroidal (B_ϕ: red) components of helical magnetic fields with different pitch profiles are shown in Fig. 6(b). The toroidal magnetic fields become zero at the center of the jet as shown by red lines in Fig. 6(b). The structure of the helical magnetic field with constant pitch ($\alpha = 1$) is shown with solid lines in Fig. 6(b). To date, simulations with the constant pitch ($\alpha = 1$) with $b = 200$ are performed using $r_{\rm jet} = 20, 40, 80, 120\Delta$ [61,67]. Here b is dumping factor of the magnetic fields outside the jet.

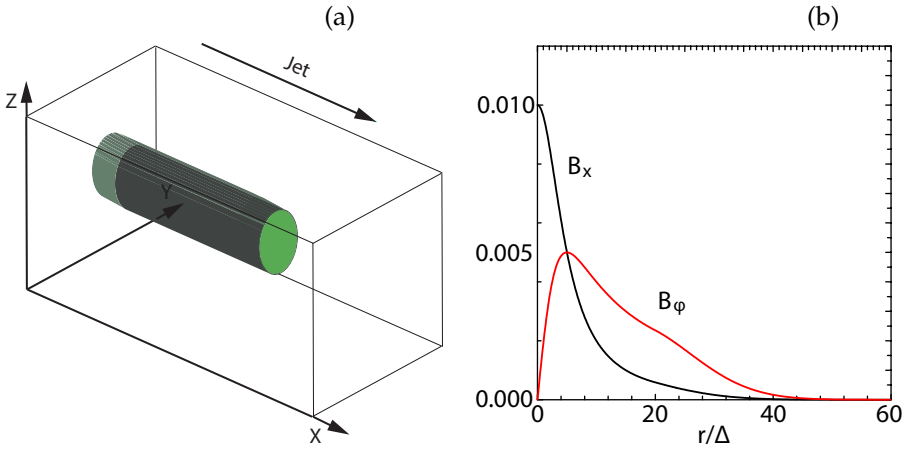

Figure 6. Panel (a) shows a schematic simulation setup: a global jet setup. The jet is injected at $x = 100\Delta$ with the jet radius $r_{\rm jt}$ at the center of the $y-z$ plane (not scaled). Panel (b) shows the helical magnetic fields, B_x(black), B_ϕ(red) with $B_0 = 0.01$ for the pitch profile $\alpha = 1.0$ with damping functions outside the jet with $b = 200.0$. The jet boundary is located at $r_{\rm jet} = 20\Delta$ [61]. So far simulations are performed with $r_{\rm jet} = 20, 40, 80, 120\Delta$ [67].

At the jet orifice, the helical magnetic field is implemented without the motional electric fields. This corresponds to a toroidal magnetic field generated self-consistently by jet particles moving along $+x$-direction. The structure of the jet formation region is more complicated than what is implemented in the PIC simulations at the present time (e.g., [69,70]).

4.2. Helically Magnetized Global Jet Simulations with Larger Jet Radii

In this section we explore how the helical magnetic field modifies jet evolution using a short system before performing larger-scale simulations. A schematic of the simulation injection setup is shown in Fig. 6 (2) [61,67]. The jet and ambient (electron) plasma number density measured in the simulation frame is $n_{\rm jt} = 8$ and $n_{\rm am} = 12$, respectively. This set of density of jet and ambient plasmas is used in these simulations [56,61,63]

In the simulations, the electron skin depth $\lambda_{\rm s} = c/\omega_{\rm pe} = 10.0\Delta$, where c is the speed of light ($c = 1$), $\omega_{\rm pe} = (e^2 n_{\rm am}/\epsilon_0 m_{\rm e})^{1/2}$ is the electron plasma frequency, and the electron Debye length for the ambient electrons is $\lambda_{\rm D} = 0.5\Delta$. The jet–electron thermal velocity is $v_{\rm jt,th,e} = 0.014c$ in the jet reference frame. The electron thermal velocity in the ambient plasma is $v_{\rm am,th,e} = 0.03c$, and ion thermal velocities are smaller by $(m_{\rm i}/m_{\rm e})^{1/2}$. Simulations were performed using an electron–positron ($e^{\pm}$) plasma or an electron–proton ($e^- - p^+$ with $m_{\rm p}/m_{\rm e} = 1836$) plasma for the jet Lorentz factor of 15 and with the ambient plasma at rest ($v_{\rm am} = 0$).

In these short system simulations, a numerical grid with $(L_x, L_y, L_z) = (645\Delta, 131\Delta, 131\Delta)$ (simulation cell size: $\Delta = 1$) is used imposing periodic boundary conditions in transverse directions

Preprints (www.preprints.org) | NOT PEER-REVIEWED | Posted: 16 November 2018 doi:10.20944/preprints201811.0374.v1

with jet radius $r_{\rm jt} = 20\Delta$ [61]. In this review all simulation parameters are maintained as described above except jet radius and simulation size (adjusted based on the jet radius). Simulations are performed using with larger jet radii $r_{\rm jt} = 40\Delta$, 80Δ, and 120Δ. These small system simulations utilize a numerical grid with $(L_x, L_y, L_z) = (645\Delta, 257\Delta, 257\Delta), (645\Delta, 509\Delta, 509\Delta), (645\Delta, 761\Delta, 761\Delta)$ (simulation cell size: $\Delta = 1$). The cylindrical jet with jet radius $r_{\rm jt} = 40\Delta$, 80Δ, and 120Δ is injected in the middle of the $y-z$ plane $((y_{\rm jc}, z_{\rm jc}) = (129\Delta, 129\Delta), (252\Delta, 252\Delta), (381\Delta, 381\Delta))$ at $x = 100\Delta$, respectively. The largest jet radius ($r_{\rm jt} = 120\Delta$) is larger than that ($r_{\rm jt} = 100\Delta$) in [56], but the simulation length is much shorter ($L_{\rm x} = 2005\Delta$).

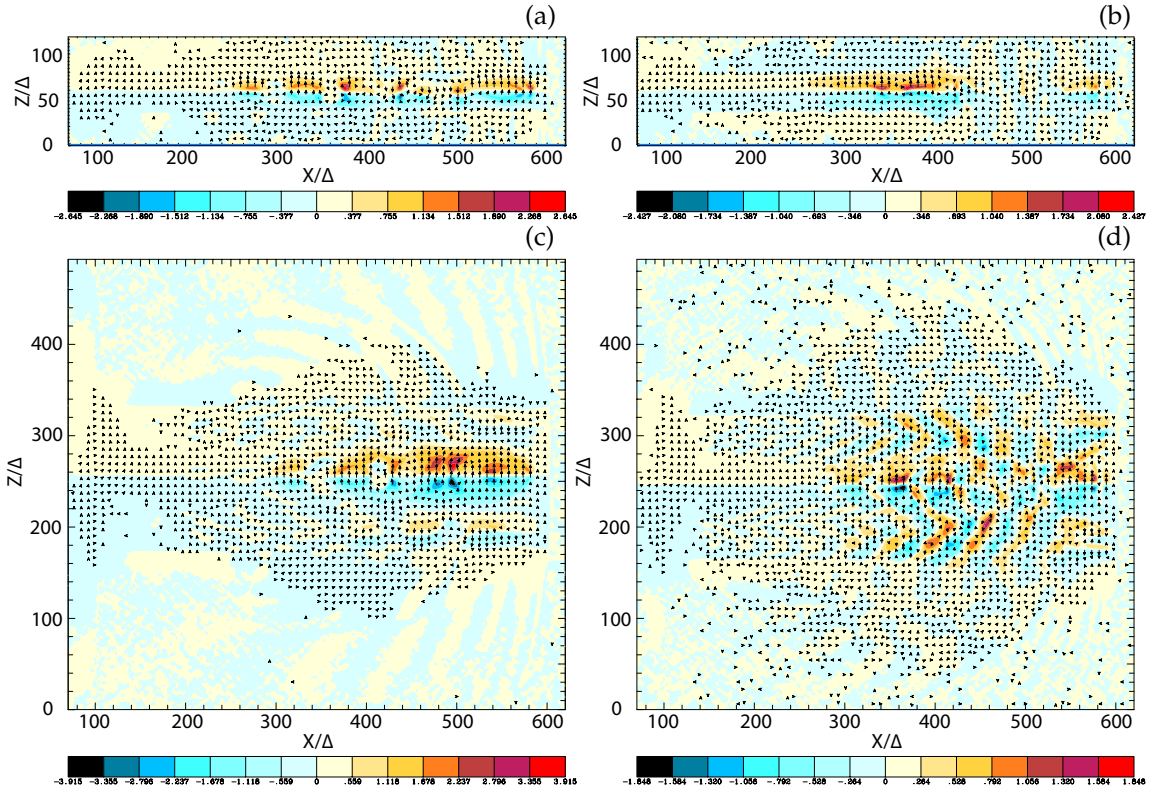

Figure 7. Isocontour plots of the azimuthal component of magnetic field B_y intensity at the center of the jets for $e^- - p^+$ ((a) and (c)) $e^\pm$ ((b) and (d)) jets; with $r_{\rm jet} = 20\Delta$ ((a) and (b)) $r_{\rm jet} = 80\Delta$ ((c) and (d)) at time $t = 500\omega_{\rm pe}^{-1}$. The disruption of helical magnetic fields are caused by instabilities and/or reconnection. The max/min numbers of panels are (a) ± 2.645, (b) ± 2.427, (c) ± 3.915, (d) ± 1.848. Adapted from Fig. 1 in Nishikawa et al. [67].

In the simulations the Initial magnetic field amplitude parameter $B_0 = 0.1c$, ($\sigma = B^2/n_{\rm e}m_{\rm e}\gamma_{\rm jet}c^2 = 2.8 \times 10^{-3}$ is used, and $a = 0.25 * r_{\rm jt}$. The helical field structure inside the jet is defined by Equations (1) and (2). For the magnetic fields outside the jet, a damping function $\exp\left[-(r - r_{\rm jt})^2/b\right]$ $(r \geq r_{\rm jt})$ is imposed on Equations (1) and (2) with the tapering parameter $b = 200$. The final profiles of the helical magnetic field components are similar to that in the case where jet radius $r_{\rm jt} = 20\Delta$, the only difference is $a = 0.25 * r_{\rm jt}$. as shown in Figure 6(b).

Figure 7 shows the y component of the magnetic field (B_y) in the jet radius with $r_{\rm jet} = 20\Delta$ and 80Δ. The initial helical magnetic field (left-handed; clockwise viewed from the jet front) is enhanced and disrupted due to the instabilities for both cases.

Even shorter simulation systems are used, the growing instabilities are affected by the helical magnetic fields. The simple recollimation shock generated in the small jet radius is shown in Figs. 7(a) and 7(b). The currents generated by instabilities in jets determin these complicated patterns of $B_{\rm y}$ as shown in Fig. 7. The larger jet radius contributes more modes of instabilities to grow in the jets, which make the jet structures more complicated. In order to investigate the full development of instabilities and jets with helical magnetic fields longer simulations are required.

Preprints (www.preprints.org) | NOT PEER-REVIEWED | Posted: 16 November 2018 doi:10.20944/preprints201811.0374.v1

In order to present particle acceleration the Lorentz factor of jet electrons is plotted in the cases with $r_{\rm jet} = 120\Delta$ as shown in Fig. 8. These patterns of Lorentz factor coincide with the changing directions of local magnetic fields in the y direction that are generated by the kinetic instabilities such as the Weibel instability, kKHI, and MI. The directions of the magnetic fields are indicated by the arrows (black spots) in the $x-z$ plane, which can be seen with magnification. The directions of magnetic fields are determined by the generated instabilities. The structures at the edge of jets are generated by the kKHI. The plots of Lorentz factor in the $y-z$ plane show the MI in the circular edge of the jets (not shown).

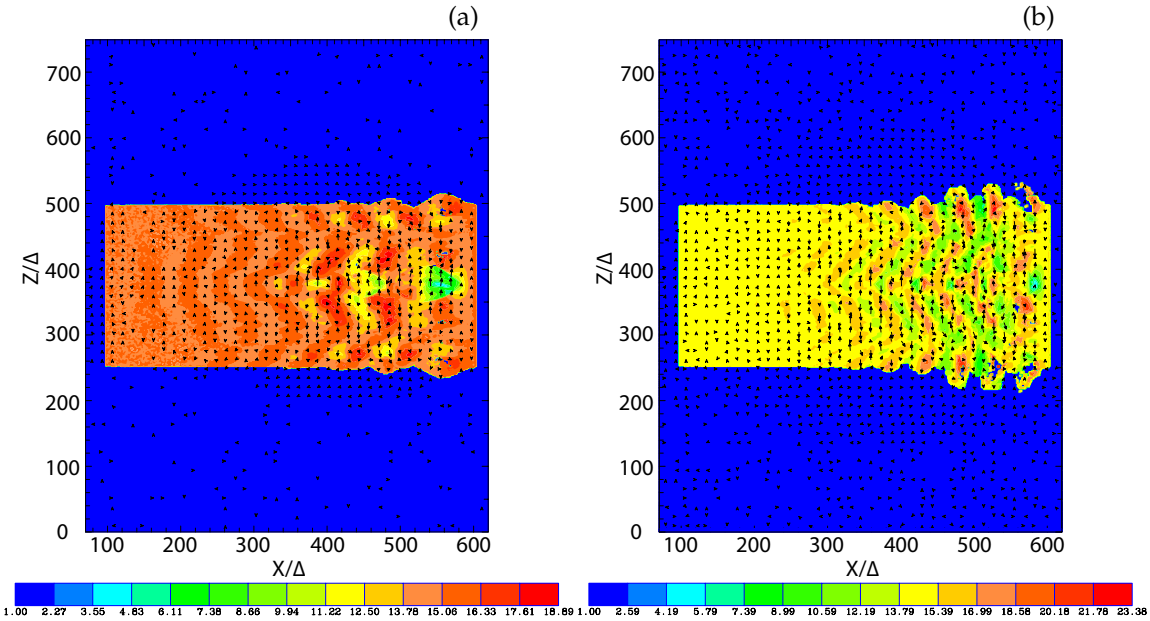

Figure 8. Panels (a) and (b) show 2D plot of the Lorentz factor of jet electrons for $e^- - p^+$ (a) and $e^\pm$ (b) jet with $r_{\rm jet} = 120\Delta$ at time $t = 500\omega_{\rm pe}^{-1}$. The arrows (black spots) show the magnetic fields in the $x-z$ plane. Adapted from Fig. 3 in Nishikawa et al. [67].

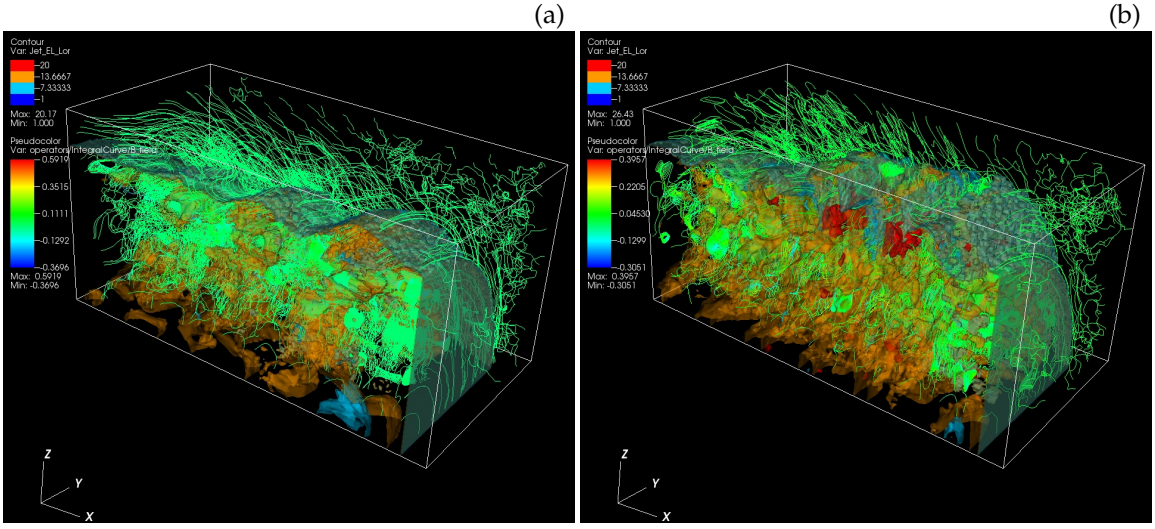

Figure 9. Panels show 3D iso-surface plots of the Lorentz factor of jet electrons for $e^- - p^+$ (a) and $e^\pm$ (b) jet with $r_{\rm jet} = 120\Delta$ at time $t = 500\omega_{\rm pe}^{-1}$. The lines show the magnetic field stream lines in the quadrant of the front part of jets. The color scales for contour (upper left): red 20.0; orange 13.67; right blue 7.33. blue 1. The color scales of streaming lines (a) (5.92, 3.52, 0.174, -1.29, -3.70) $\times 10^{-1}$; (b) (3.96, 2.21, 0.453, -1.30, -3.05) $\times 10^{-1}$. Adapted from Fig. 4 in Nishikawa et al. [67].

Preprints (www.preprints.org) | NOT PEER-REVIEWED | Posted: 16 November 2018 doi:10.20944/preprints201811.0374.v1

Figure 9 shows the isosurface of Lorentz factor of jet electrons for $e^- - p^+$ (a) and $e^\pm$ (b) jet. 3D iso-surface of the averaged jet electron Lorentz factor in a quadrant of the jet front ($320 \leq x/\Delta \leq 620$, $381 \leq y, z/\Delta \leq 531$) shows where jet electrons are accelerated shown with reddish color locally. The cross sections and surfaces of jets show complicated patterns that are generated by mixed instabilities with the magnetic field lines.

In both cases with the jet radii larger than $r_{\rm jet} = 80\Delta$, at the jet surfaces kKHI and MI are generated, and inside the jets the Weibel instability is generated with a kink-like instability, in particular in the electron-proton jet. How the growth of kink-like instabilities depends on the helical magnetic fields requires further investigations using different parameters including a which determines the structure of helical magnetic fields in Eqs. (2) and (3). Furthermore, the pitch parameter α is also necessary to be investigated using Eq. (1)

Recently, Dieckmann et al. [57] investigated the expansion of a cloud of electrons and positrons with the temperature 400 keV that propagates at the mean speed 0.9c (c : speed of light) through an initially unmagnetized electron-proton plasma with a particle-in-cell (PIC) simulation. They found a mechanism that collimates the pair cloud into a jet. A filamentation instability develops between the protons at rest and the moving positrons. The generated magnetic field collimates the positrons and drives an electrostatic shock into the electron-proton plasma. The electrons and positrons of the cloud expanded rapidly due to their large temperature, which decreased the density of the cloud. A filamentation instability developed between the protons at rest and the positrons in the interval where the latter were still dense. It is noted that it is difficult to distinguish the filament instability from the kKHI, which is shown in the simulation where electron-positron jet is injected into an electron-positron ambient [56]. This instability expelled the protons from large areas, which were then filled with positrons. Magnetic fields grew only in those locations where protons and rapidly streaming positrons are present, which confines the magnetic field to small spatial span. The effect of the filamentation instability and the resulting magnetic field are to push the protons away from the regions with no proton. The instability and the magnetic field follow the pushed protons and, hence, the filament grows in size. The largest filament grew along the refecting boundary of their simulation and the magnetic field that push the protons out, became a stable magnetic piston. This filament is the largest one because the density of the cloud is largest close to the boundary and because it was aligned with the flow direction of the pair cloud. The large pool of directed flow energy is converted to magnetic field energy by the filament instability. Similar expansion of electron-positron jet plasmas was observed in the global jets without helical magnetic fields [56].

The filament evolved into a pair jet that was separated magnetically from the expelled and shocked ambient plasma. The front of the jet propagated with the speed 0.15c along the boundary and expanded laterally at a speed that amounted to 0.03c. The growth of the filament was limited by their simulation box size and by the limited cloud size; a decrease of the ram pressure would inevitably lead to a weakening of the filamentation instability and to a collapse of the jet. But it appears that, as long as the pair cloud has enough ram pressure, the filaments can grow to arbitrarily large sizes if the filamentation instability develops between a pair cloud and an electron-proton plasma at least for plasma parameters similar to those used here.

4.3. Reconnection in Jets with Helical Magnetic Fields

Reconnection is ubiquitous in solar and magnetosphere plasmas, and it is an important additional particle acceleration mechanism for AGN and gamma-ray burst jets [e.g., 71]. In spite of the extensive research on reconnection, most of all reconnection simulations have been performed with the Harris sheet [72]. where the unperturbed magnetic fields $\mathbf{B}$ are anti-parallel ($\mathbf{B} = -\tanh(x)\mathbf{e}_y$). The energy release and particle acceleration during reconnection have been proposed as a mechanism for producing high-energy emissions and cosmic rays [e.g., 71,73]. It should be noted that the stored magnetic field energy in anti-parallel magnetic field in the slab model is not consistent with the

Preprints (www.preprints.org) | NOT PEER-REVIEWED | Posted: 16 November 2018 doi:10.20944/preprints201811.0374.v1

helical magnetic fields in relativistic jets, therefore a realistic argument on particle acceleration due to reconnection requires consideration of helical magnetic field in jets.

The importance of reconnection in jets has been proposed previously, but no kinetic simulation of global jets with helical magnetic fields has been performed before with the exception of our own simulations [61,67].

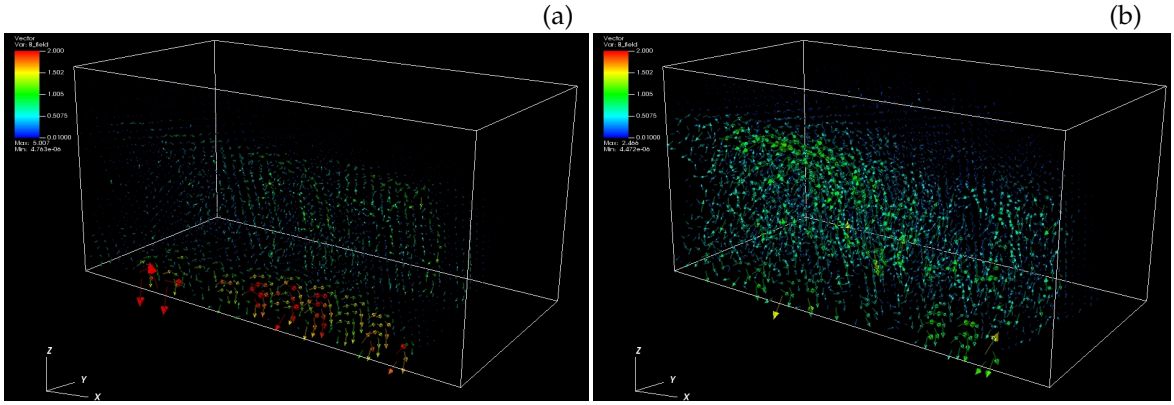

Figure 10. Panels show 3D vector plots of the magnetic fields for $e^- - p^+$ (a) and $e^\pm$ (b) jet with $r_{\rm jet} = 120\Delta$ at time $t = 500\omega_{\rm pe}^{-1}$. The colors show the strength of the magnetic fields in the quadrant of the front part of jets

Figure 10 shows the vectors of magnetic fields in the quadrant of the front part of jets as shown in Fig. (10). Unfortunately, these vectors do not show the changes in direction which may reveal reconnection sites. In order to find the reconnection region, it is necessary to analyze the critical points.

Critical points (CPs) or magnetic nulls are the points where the magnitude of magnetic field vector vanishes [74]. These points may be characterized by the behaviour of nearby magnetic field curves or surfaces. The set of curves or surfaces that end on CPs is of special interest because it defines the behaviour of the magnetic field in the neighborhood of CP.

The usual magnetic field configuration satisfies the hyperbolic conditions in which the vector field system has nonzero real part of eigenvalues. The bifurcation (the topological change) present the magnetic reconnection in the magnetic field. Thus the particular sets of CPs, curves, and surfaces can be used to define a skeleton that uniquely characterizes the magnetic field [74]. In order to investigate the location of reconnection and its evolution, the method described in Cai, Nishikawa and Lembege (2007) [74] needs to be employed in the future work.

5. Discussions

Simulations of relativistic jets have been investigated extensively from the Weibel instability in slab mode, instabilities in velocity-shears and recently the geometry of jets has been taken into account within more realistic simulations.

The global jet simulations with large jet radii show the importance of a larger jet radius in PIC simulations for investigating in-tandem the macroscopic processes incorporated in RMHD simulations. Due to mixed modes of generated instabilities, jet electrons in phase space show little or no bunching in comparison to those with smaller jet radius $r_{\rm jet} = 20\Delta$. Consequently, recollimation shocks occur rather in the center of jets, which is dependent on the value of parameter of helical magnetic field structure parameter a. It requires further investigation with even larger radii of jets.

These simulations show that the energy stored in helical magnetic fields is released due to the excitations of kinetic instabilities such as kKHI, MI and the Weibel instability with kink-like instability. Consequently, electrons are accelerated and turbulent magnetic fields are generated, which provide polarity.

MacDonald & Marscher [3] have developed a radiative transfer scheme that allows the Turbulent Extreme Multi-Zone (TEMZ) code to produce simulated images of the time-dependent linearly and

circularly polarized intensity at different radio frequencies. Using this technique with the simulation results, synthetic polarized emission maps have been obtained that highlight the linear and circular polarization expected within the above PIC models. This algorithm is currently being refined to account for slow-light interpolation through our PIC simulations.

Since the power of supercomputers is growing rapidly, very large simulations of global jets could be performed, which will provide new insights on jet evolution including reconnection and associated phenomena such as flares and high-energy particle generation.

Supplementary Materials: The following are available online at www.mdpi.com/link, Figure S1: title, Table S1: title, Video S1: title.

Acknowledgments: This work is supported by NSF AST-0908010, AST-0908040, NASA-NNX09AD16G, NNX12AH06G, NNX13AP-21G, and NNX13AP14G grants. The work of J.N. and O.K. has been supported by Narodowe Centrum Nauki through research project DEC-2013/10/E/ST9/00662. Y.M. is supported by the ERC Synergy Grant "BlackHoleCam - Imaging the Event Horizon of Black Holes" (Grant No. 610058). M.P. acknowledges support through grant PO 1508/1-2 of the Deutsche Forschungsgemeinschaft. Simulations were performed using Pleiades and Endeavor facilities at NASA Advanced Supercomputing (NAS), and using Gordon and Comet at The San Diego Supercomputer Center (SDSC), and Stampede at The Texas Advanced Computing Center, which are supported by the NSF. This research was started during the program "Chirps, Mergers and Explosions: The Final Moments of Coalescing Compact Binaries" at the Kavli Institute for Theoretical Physics, which is supported by the National Science Foundation under grant No. PHY05-51164. The first velocity shear results using an electron−positron plasma were obtained during the Summer Aspen workshop "Astrophysical Mechanisms of Particle Acceleration and Escape from the Accelerators" held at the Aspen Center for Physics (1–15 September 2013).

Author Contributions: K. -I. Nishikawa: Perform simulations, analyze the data and prepare a manuscript; Y. Mizuno: Compare with RMHD simulations; J. L. Gómez: Contribute for comparing simulation results to observations; J. Niemiec: Contribute modifying the code for this research; O. Kobzar; Modify the code for this simulation; M. Pohl: Overlook the simulation results; J. L. Gómez : Contribute on comparisons with observations; I. Duţan: Perform some of simulations for this research; A. Meli: Critical reading and discussion on this research; H. Sol: Essential suggestions for this research; D. H. Hartmann: Useful discussions for this research

Conflicts of Interest: The authors declare no conflict of interest.

1. Hawley, J.; Fendt, C.; Hardcastle, M.; Nokhrima, E.; Tchekhovskoy, A. Disks and Jets **2015**. *191*. doi:https://doi.org/10.1007/s1121.
2. Pe'er, A. Energetic and Broad Band Spectral Distribution of Emission from Astronomical Jets. *Space Science Reviews* **2014**, *183*, 371–403. doi:10.1007/s11214-013-0001-y.
3. MacDonald, N.R.; Marscher, A.P. Faraday Conversion in Turbulent Blazar Jets. *The Astrophysical Journal* **2018**, *862*, 58.
4. Silva, L.O.; Fonseca, R.A.; Tonge, J.W.; Dawson, J.M.; Mori, W.B.; Medvedev, M.V. Interpenetrating Plasma Shells: Near-Equipartition Magnetic Field Generation and Nonthermal Particle Acceleration. *The Astrophysical Journal Letters* **2003**, *596*, L121.
5. Nishikawa, K.I.; Hardee, P.; Richardson, G.; Preece, R.; Sol, H.; Fishman, G.J. Particle Acceleration in Relativistic Jets Due to Weibel Instability. *ApJ* **2003**, *595*, 555–563.
6. Frederiksen, J.T.; Hededal, C.B.; Haugbølle, T.; Nordlund, Å. Magnetic Field Generation in Collisionless Shocks: Pattern Growth and Transport. *The Astrophysical Journal Letters* **2004**, *608*, L13.
7. Hededal, C.B.; Haugbølle, T.; Frederiksen, J.T.; Nordlund, Å. Non-Fermi Power-Law Acceleration in Astrophysical Plasma Shocks. *The Astrophysical Journal Letters* **2004**, *617*, L107.
8. Hededal, C.B.; Nishikawa, K.I. The Influence of an Ambient Magnetic Field on Relativistic collisionless Plasma Shocks. *The Astrophysical Journal Letters* **2005**, *623*, L89.
9. Nishikawa, K.I.; Hardee, P.; Richardson, G.; Preece, R.; Sol, H.; Fishman, G.J. Particle Acceleration and Magnetic Field Generation in Electron-Positron Relativistic Shocks. *The Astrophysical Journal* **2005**, *622*, 927.
10. Jaroschek, C.H.; Lesch, H.; Treumann, R.A. Ultrarelativistic Plasma Shell Collisions in γ-Ray Burst Sources: Dimensional Effects on the Final Steady State Magnetic Field. *The Astrophysical Journal* **2005**, *618*, 822.
11. Nishikawa, K.I.; Hardee, P.E.; Hededal, C.B.; Fishman, G.J. Acceleration Mechanics in Relativistic Shocks by the Weibel Instability. *The Astrophysical Journal* **2006a**, *642*, 1267.

12. Nishikawa, K.I.; Hardee, P.; Hededal, C.; Richardson, G.; Preece, R.; Sol, H.; Fishman, G. Particle acceleration, magnetic field generation, and emission in relativistic shocks. *Advances in Space Research* **2006b**, *38*, 1316 – 1319. Galactic and Extragalactic Astrophysics, doi:https://doi.org/10.1016/j.asr.2005.01.036.
13. Nishikawa, K.I.; Mizuno, Y.; Fishman, G.J.; Hardee, P. Particle Acceleration, Magnetic Field Generation, and Associated Emission in Collisionless Relativistic Jets. *International Journal of Modern Physics D* **2008**, *17*, 1761–1767, [0801.4390]. doi:10.1142/S0218271808013388.
14. Spitkovsky, A. On the Structure of Relativistic Collisionless Shocks in Electron-Ion Plasmas. *The Astrophysical Journal Letters* **2008**, *673*, L39.
15. Spitkovsky, A. Particle Acceleration in Relativistic Collisionless Shocks: Fermi Process at Last? *The Astrophysical Journal Letters* **2008**, *682*, L5.
16. Chang, P.; Spitkovsky, A.; Arons, J. Long-Term Evolution of Magnetic Turbulence in Relativistic Collisionless Shocks: Electron-Positron Plasmas. *The Astrophysical Journal* **2008**, *674*, 378.
17. Dieckmann, M.E.; Shukla, P.K.; Drury, L.O.C. The Formation of a Relativistic Partially Electromagnetic Planar Plasma Shock. *The Astrophysical Journal* **2008**, *675*, 586–595, [astro-ph/0702055]. doi:10.1086/525516.
18. Nishikawa, K.I.; Niemiec, J.; Hardee, P.E.; Medvedev, M.; Sol, H.; Mizuno, Y.; Zhang, B.; Pohl, M.; Oka, M.; Hartmann, D.H. Weibel Instability and Associated Strong Fields in a Fully Three-Dimensional Simulation of a Relativistic Shock. *The Astrophysical Journal Letters* **2009**, *698*, L10.
19. Martins, S.F.; Fonseca, R.A.; Silva, L.O.; Mori, W.B. Ion Dynamics and Acceleration in Relativistic Shocks. *The Astrophysical Journal Letters* **2009**, *695*, L189.
20. Nishikawa, K.I.; Niemiec, J.; Medvedev, M.; Zhang, B.; Hardee, P.; Nordlund, A.; Frederiksen, J.; Mizuno, Y.; Sol, H.; Pohl, M.; Hartmann, D.; Oka, M.; Fishman, G. Radiation from relativistic shocks in turbulent magnetic fields. *Advances in Space Research* **2011**, *47*, 1434 – 1440. Neutron Stars and Gamma Ray Bursts, doi:https://doi.org/10.1016/j.asr.2011.01.032.
21. Choi, E.J.; Min, K.; Nishikawa, K.I.; Choi, C.R. A study of the early-stage evolution of relativistic electron-ion shock using three-dimensional particle-in-cell simulations. *Physics of Plasmas* **2014**, *21*, 072905. doi:10.1063/1.4890479.
22. Ardaneh, K.; Cai, D.; Nishikawa, K.I.; Lembége, B. Collisionless Weibel Shocks and Electron Acceleration in Gamma-Ray Bursts. *The Astrophysical Journal* **2015**, *811*, 57.
23. Ardaneh, K.; Cai, D.; Nishikawa, K.I. Collisionless Electron-ion Shocks in Relativistic Unmagnetized Jet-ambient Interactions: Non-thermal Electron Injection by Double Layer. *The Astrophysical Journal* **2016**, *827*, 124.
24. Grassi, A.; Grech, M.; Amiranoff, F.; Macchi, A.; Riconda, C. Radiation-pressure-driven ion Weibel instability and collisionless shocks. *PhyRevE* **2017**, *96*, 033204, [arXiv:physics.plasm-ph/1705.05402]. doi:10.1103/PhysRevE.96.033204.
25. Iwamoto, M.; Amano, T.; Hoshino, M.; Matsumoto, Y. Precursor Wave Emission Enhanced by Weibel Instability in Relativistic Shocks. *The Astrophysical Journal* **2018**, *858*, 93.
26. Takamoto, M.; Matsumoto, Y.; Kato, T.N. Magnetic Field Saturation of the Ion Weibel Instability in Interpenetrating Relativistic Plasmas. *The Astrophysical Journal Letters* **2018**, *860*, L1.
27. Weibel, E. Spontaneously Growing Transverse Waves in a Plasma Due to an Anisotropic Velocity Distr. *PhRvL* **1959**, *2*, 83–84. doi:10.1103/PhysRevLett.2.83.
28. Medvedev, M.V.; Loeb, A. Generation of Magnetic Fields in the Relativistic Shock of Gamma-Ray Burst Sources. *The Astrophysical Journal* **1999**, *526*, 697.
29. Medvedev, M.V.; Zakutnyaya, O.V. Magnetic Fields and Cosmic Rays in GRBs: A Self-Similar Collisionless Foreshock. *The Astrophysical Journal* **2009**, *696*, 2269.
30. Hoshino, M.; Shimada, N. Nonthermal Electrons at High Mach Number Shocks: Electron Shock Surfing Acceleration. *The Astrophysical Journal* **2002**, *572*, 880.
31. Amano, T.; Hoshino, M. Electron Injection at High Mach Number Quasi-perpendicular Shocks: Surfing and Drift Acceleration. *The Astrophysical Journal* **2007**, *661*, 190.
32. Amano, T.; Hoshino, M. Electron Shock Surfing Acceleration in Multidimensions: Two-Dimensional Particle-in-Cell Simulation of Collisionless Perpendicular Shock. *The Astrophysical Journal* **2009**, *690*, 244.
33. Sironi, L.; Giannios, D. A Late-time Flattening of Light Curves in Gamma-Ray Burst Afterglows. *The Astrophysical Journal* **2013**, *778*, 107.

34. Guo, X.; Sironi, L.; Narayan, R. Non-thermal Electron Acceleration in Low Mach Number Collisionless Shocks. I. Particle Energy Spectra and Acceleration Mechanism. *The Astrophysical Journal* **2014**, *794*, 153.
35. Sironi, L.; Petropoulou, M.; Giannios, D. Relativistic jets shine through shocks or magnetic reconnection? *Monthly Notices of the Royal Astronomical Society* **2015**, *450*, 183–191. doi:10.1093/mnras/stv641.
36. Bret, A.; Alvaro, E.P. Robustness of the filamentation instability as shock mediator in arbitrarily oriented magnetic field. *Physics of Plasmas* **2011**, *18*, 080706–080706, [arXiv:astro-ph.HE/1106.3477]. doi:10.1063/1.3609794.
37. Buneman, O. Tristan. *Computer Space Plasma Physics: Simulation Techniques and Software* **1993**, *1*, 67–100.
38. Niemiec, J.; Pohl, M.; Stroman, T.; Nishikawa, K.I. Production of Magnetic Turbulence by Cosmic Rays Drifting Upstream of Supernova Remnant Shocks. *The Astrophysical Journal* **2008**, *684*, 1174.
39. Ramirez-Ruiz, E.; Nishikawa, K.I.; Hededal, C.B. $e^{\pm}$ Pair Loading and the Origin of the Upstream Magnetic Field in GRB Shocks. *The Astrophysical Journal* **2007**, *671*, 1877.
40. Mizuno, Y.; Lyubarsky, Y.; Nishikawa, K.I.; Hardee, P.E. Three-Dimensional Relativistic Magnetohydrodynamic Simulations of Current-Driven Instability. I. Instability of a Static Column. *The Astrophysical Journal* **2009**, *700*, 684.
41. Spitkovsky, A. Simulations of relativistic collisionless shocks: shock structure and particle acceleration. Astrophysical Sources of High Energy Particles and Radiation; Bulik, T.; Rudak, B.; Madejski, G., Eds., 2005, Vol. 801, *American Institute of Physics Conference Series*, pp. 345–350, [astro-ph/0603211]. doi:10.1063/1.2141897.
42. D'Angelo, N. Kelvin-Helmholtz Instability in a Fully Ionized Plasma in a Magnetic Field. *The Physics of Fluids* **1965**, *8*, 1748–1750, [https://aip.scitation.org/doi/pdf/10.1063/1.1761496]. doi:10.1063/1.1761496.
43. Gruzinov, A. GRB: magnetic fields, cosmic rays, and emission from first principles? *ArXiv e-prints* **2008**, [0803.1182].
44. Mizuno, Y.; Hardee, P.; Nishikawa, K.I. Three-dimensional Relativistic Magnetohydrodynamic Simulations of Magnetized Spine-Sheath Relativistic Jets. *The Astrophysical Journal* **2007**, *662*, 835–850, [astro-ph/0703190]. doi:10.1086/518106.
45. Perucho, M.; Lobanov, A.P. Kelvin-Helmholtz Modes Revealed by the Transversal Structure of the Jet in 0836+710. Extragalactic Jets: Theory and Observation from Radio to Gamma Ray; Rector, T.A.; De Young, D.S., Eds., 2008, Vol. 386, *Astronomical Society of the Pacific Conference Series*, p. 381, [0707.2887].
46. Zhang, W.; MacFadyen, A.; Wang, P. Three-Dimensional Relativistic Magnetohydrodynamic Simulations of the Kelvin-Helmholtz Instability: Magnetic Field Amplification by a Turbulent Dynamo. *The Astrophysical Journal Letters* **2009**, *692*, L40.
47. Alves, E.P.; Grismayer, T.; Martins, S.F.; FiÃºza, F.; Fonseca, R.A.; Silva, L.O. Large-scale Magnetic Field Generation via the Kinetic Kelvin-Helmholtz Instability in Unmagnetized Scenarios. *The Astrophysical Journal Letters* **2012**, *746*, L14.
48. Nishikawa, K.I.; Hardee, P.; Zhang, B.; DuÅ£an, I.; Medvedev, M.; Choi, E.J.; Min, K.W.; Niemiec, J.; Mizuno, Y.; Nordlund, A.; Frederiksen, J.T.; Sol, H.; Pohl, M.; Hartmann, D.H. Magnetic field generation in a jet-sheath plasma via the kinetic Kelvin-Helmholtz instability. *Annales Geophysicae* **2013**, *31*, 1535–1541. doi:10.5194/angeo-31-1535-2013.
49. Liang, E.; Boettcher, M.; Smith, I. Magnetic Field Generation and Particle Energization at Relativistic Shear Boundaries in Collisionless Electron-Positron Plasmas. *The Astrophysical Journal Letters* **2013**, *766*, L19.
50. Grismayer, T.; Alves, E.P.; Fonseca, R.A.; Silva, L.O. dc-Magnetic-Field Generation in Unmagnetized Shear Flows. *Phys. Rev. Lett.* **2013**, *111*, 015005. doi:10.1103/PhysRevLett.111.015005.
51. Grismayer, T.; Alves, E.P.; Fonseca, R.A.; Silva, L.O. Theory of multidimensional electron-scale instabilities in unmagnetized shear flows. *Plasma Physics and Controlled Fusion* **2013**, *55*, 124031.
52. Liang, E.; Fu, W.; Boettcher, M.; Smith, I.; Roustazadeh, P. Relativistic Positron-Electron-Ion Shear Flows and Application to Gamma-Ray Bursts. *The Astrophysical Journal Letters* **2013**, *779*, L27.
53. Alves, E.P.; Grismayer, T.; Fonseca, R.A.; Silva, L.O. Electron-scale shear instabilities: magnetic field generation and particle acceleration in astrophysical jets. *New Journal of Physics* **2014**, *16*, 035007.
54. Alves, E.P.; Grismayer, T.; Fonseca, R.A.; Silva, L.O. Transverse electron-scale instability in relativistic shear flows. *PhRvE* **2015**, *92*, 021101, [arXiv:physics.plasm-ph/1505.06016]. doi:10.1103/PhysRevE.92.021101.

55. Nishikawa, K.I.; Hardee, P.E.; DuÅ£an, I.; Niemiec, J.; Medvedev, M.; Mizuno, Y.; Meli, A.; Sol, H.; Zhang, B.; Pohl, M.; Hartmann, D.H. Magnetic Field Generation in Core-sheath Jets via the Kinetic Kelvin-Helmholtz Instability. *The Astrophysical Journal* **2014b**, *793*, 60.
56. Nishikawa, K.I.; Frederiksen, J.T.; Nordlund, Å.; Mizuno, Y.; Hardee, P.E.; Niemiec, J.; Gómez, J.L.; Pe'er, Å.; Dutan, I.; Meli, A.; Sol, H.; Pohl, M.; Hartmann, D.H. Evolution of Global Relativistic Jets: Collimations and Expansion with kKHI and the Weibel Instability. *The Astrophysical Journal* **2016a**, *820*, 94.
57. Dieckmann, M.; Sarri, G.; Folini, D.; Walder, R.; Borghesi, M. Cocoon formation by a mildly relativistic pair jet in unmagnetized collisionless electron-proton plasma. *ArXiv e-prints* **2018**, [arXiv:astro-ph.HE/1809.10194].
58. Nishikawa, K.I.; Hardee, P.; Dutan, I.; Zhang, B.; Meli, A.; Choi, E.J.; Min, K.; Niemiec, J.; Mizuno, Y.; Medvedev, M.; Nordlund, A.; Frederiksen, J.T.; Sol, H.; Pohl, M.; Hartmann, D. Radiation from Particles Accelerated in Relativistic Jet Shocks and Shear-flows. *ArXiv e-prints* **2014**, [arXiv:astro-ph.HE/1412.7064].
59. Alves, E.P.; Zrake, J.; Fiuza, F. Efficient Nonthermal Particle Acceleration by the Kink Instability in Relativistic Jets. *ArXiv e-prints* **2018**, [arXiv:astro-ph.HE/1810.05154].
60. Blandford, R.D.; Znajek, R.L. Electromagnetic extraction of energy from Kerr black holes. *Monthly Notices of the Royal Astronomical Society* **1977**, *179*, 433–456. doi:10.1093/mnras/179.3.433.
61. Nishikawa, K.I.; Mizuno, Y.; Niemiec, J.; Kobzar, O.; Pohl, M.; Gómez, J.L.; Dutan, I.; Pe'er, A.; Frederiksen, J.T.; Nordlund, Å.; Meli, A.; Sol, H.; Hardee, P.E.; Hartmann, D.H. Microscopic Processes in Global Relativistic Jets Containing Helical Magnetic Fields. *Galaxies* **2016b**, *4*.
62. Tchekhovskoy, A. Launching of Active Galactic Nuclei Jets. *The Formation and Disruption of Black Hole Jets* **2015**, *414*, 45–82.
63. Dutan, I.; Nishikawa, K.I.; Mizuno, Y.; Niemiec, J.; Kobzar, O.; Pohl, M.; Gómez, J.L.; Pe'er, A.; Frederiksen, J.T.; Nordlund, Å.; et al.. Particle-in-cell Simulations of Global Relativistic Jets with Helical Magnetic Fields. *Proceedings of the International Astronomical Union* **2016**, *12*, 199–202. doi:10.1017/S1743921316012722.
64. Mizuno, Y.; Hardee, P.E.; Nishikawa, K.I. Spatial Growth of the Current-driven Instability in Relativistic Jets. *The Astrophysical Journal* **2014**, *784*, 167.
65. Singh, C.B.; Mizuno, Y.; de Gouveia Dal Pino, E.M. Spatial Growth of Current-driven Instability in Relativistic Rotating Jets and the Search for Magnetic Reconnection. *The Astrophysical Journal* **2016**, *824*, 48.
66. Barniol Duran, R.; Tchekhovskoy, A.; Giannios, D. Simulations of AGN jets: magnetic kink instability versus conical shocks. *Monthly Notices of the Royal Astronomical Society* **2017**, *469*, 4957–4978. doi:10.1093/mnras/stx1165.
67. Nishikawa, K.I.; Mizuno, Y.; Gómez, J.L.; Dutan, I.; Meli, A.; White, C.; Niemiec, J.; Kobzar, O.; Pohl, M.; Pe'er, A.; Frederiksen, J.T.; Nordlund, Å.; Sol, H.; Hardee, P.E.; Hartmann, D.H. Microscopic Processes in Global Relativistic Jets Containing Helical Magnetic Fields: Dependence on Jet Radius. *Galaxies* **2017**, *5*.
68. Mizuno, Y.; Gomez, J.L.; Nishikawa, K.I.; Meli, A.; Hardee, P.E.; Rezzolla, L. Recollimation Shocks in Magnetized Relativistic Jets. *The Astrophysical Journal* **2015**, *809*, 38.
69. Broderick, A.E.; Loeb, A. Imaging the Black Hole Silhouette of M87: Implications for Jet Formation and Black Hole Spin. *The Astrophysical Journal* **2009**, *697*, 1164.
70. Mościbrodzka, M.; Dexter, J.; Davelaar, J.; Falcke, H. Faraday rotation in GRMHD simulations of the jet launching zone of M87. *Monthly Notices of the Royal Astronomical Society* **2017**, *468*, 2214–2221. doi:10.1093/mnras/stx587.
71. Giannios, D.; Uzdensky, D.A.; Begelman, M.C. Fast TeV variability in blazars: jets in a jet. *Monthly Notices of the Royal Astronomical Society: Letters* **2009**, *395*, L29–L33. doi:10.1111/j.1745-3933.2009.00635.x.
72. Harris, E.G. On a plasma sheath separating regions of oppositely directed magnetic field. *Il Nuovo Cimento* **1962**, *23*, 115–121. doi:10.1007/BF02733547.
73. Barniol Duran, R.; Leng, M.; Giannios, D. An anisotropic minijets model for the GRB prompt emission. *Monthly Notices of the Royal Astronomical Society: Letters* **2016**, *455*, L6–L10. doi:10.1093/mnrasl/slv140.
74. Cai, D.; Nishikawa, K.I.; Lembege, B. Visualization of Tangled Vector Field Topology and Global Bifurcation of Magnetospheric Dynamics. Advanced Methods for Space Simulations, 2007.

Sample Availability: Samples of the compounds ..... are available from the authors.